Atmos. Meas. Tech. Discuss., https://doi.org/10.5194/amt-2017-429
Manuscript under review for journal Atmos. Meas. Tech.
Discussion started: 20 December 2017

Atmospheric Measurement Techniques Discussions

Impact of the Ozone Monitoring Instrument Row Anomaly on the Long-term Record of Aerosol Products

Omar Torres[1], Pawan K. Bhartia[1], Hiren Jethva[2,1], Changwoo Ahn[3,1]

[1]Atmospheric Chemistry and Dynamics Laboratory, NASA Goddard Space Flight Center, Greenbelt, MD, 20770, USA
[2]GESTAR/Universities Space Research Association, Columbia, MD, 21046, USA
[3]Science Systems and Applications, Inc., 10210 Greenbelt Road, Lanham, Maryland 20706

Correspondence to: Omar Torres (Omar.O.Torres@nasa.gov)

Abstract

Since about three years after the launch the Ozone Monitoring Instrument (OMI) on the EOS-Aura satellite, the sensor's viewing capability has been affected by what is believed to be an internal obstruction that has reduced OMI's spatial coverage. It currently affects about half of the instrument's sixty viewing positions. In this work we carry out an analysis to assess the effect of the reduced spatial coverage on the monthly average values of retrieved aerosol optical depth (AOD), single scattering albedo (SSA), and the UV Aerosol Index (UVAI) using the 2005-2007 three-year period prior to the onset of the row anomaly. Regional monthly average values calculated using viewing positions 1 through 30 were compared to similarly obtained values using positions 31 thru 60 with the expectation of finding close agreement between the two calculations. As expected, mean monthly values of AOD and SSA obtained with these two scattering-angle-dependent sub-sets of OMI observations were in agreement over regions where carbonaceous or sulphate aerosol particles are the predominant aerosol type. Over arid regions, however, where desert dust is the main aerosol type, significant differences between the two sets of calculated regional mean values of AOD were observed. As it turned out, the difference in retrieved desert dust AOD between the scattering-angle dependent observation subsets was due to the incorrect representation of desert dust scattering phase function. A sensitivity analysis using radiative transfer calculations demonstrated that the source of the observed AOD bias was the spherical shape assumption of desert dust particles. A similar analysis in terms of UVAI yielded large differences in the monthly mean values for the two sets of calculations over cloudy regions. On the contrary, in arid regions with minimum cloud presence, the resulting UVAI monthly average values for the two sets of observations were in very close agreement. The discrepancy under cloudy conditions was found to be caused by the parameterization of clouds as opaque Lambertian reflectors. When properly accounting for cloud scattering effects using Mie Theory, the observed UVAI angular bias was significantly reduced. The analysis discussed here has uncovered important algorithmic deficiencies associated with the model representation of the angular dependence of scattering effects of desert dust aerosols and cloud droplets. The resulting improvements in the handling of desert dust and cloud scattering have been incorporated in an improved version of the OMAERUV algorithm.

Atmos. Meas. Tech. Discuss., https://doi.org/10.5194/amt-2017-429
Manuscript under review for journal Atmos. Meas. Tech.
Discussion started: 20 December 2017

Atmospheric Measurement Techniques Discussions

1 Introduction

The Ozone Monitoring Instrument (OMI) on the EOS-Aura satellite has been circling the Earth on an ascending orbit for over a decade since its launch in July 2004 [*Levelt et al.*, 2006]. OMI's hyper-spectral radiance measurements (270-500 nm) cover a 2400 km across-track swath, scanning West-to-East at sixty viewing positions or rows, providing global daily coverage. These observations are used in retrieval algorithms to derive concentration of total ozone [*McPeters et al.*, 2015]; NO_2 and SO_2 [*Li et al.*, 2013; *Boersma et al.*, 2011; *Krotkov et al.*, 2016]; CH_2O [*González et al.*, 2015] as well as aerosol properties [*Torres et al.*, 2007; 2013] and clouds [*Acarreta et al.*, 2004; *Joiner and Vasilkov*, 2006].

The OMI near UV algorithm (OMAERUV) uses observations at 354 and 388 nm to derive aerosol optical depth (AOD) and single scattering albedo (SSA) in addition to the qualitative UV Aerosol Index (UVAI) [*Torres et al.*, 2007; 2013]. OMAERUV quantitative aerosol products have been evaluated by comparison to independent ground-based observations [*Torres et al.*, 2007; 2013; *Ahn et al., 2014; Jethva et al., 2014, Zhang et al., 2016*], airborne measurements [*Livingston et al.*, 2009] as well as to other satellite measurements [*Ahn et al., 2008; 2014; Gassó and Torres*, 2016].

Since early 2008, a reduction in OMI's spatial coverage associated with the onset of the so-called *row anomaly* has been observed. The row anomaly is believed to be the result of a physical obstruction that affects both Earth radiance and solar flux OMI measurements. Although in June 2007 only two of OMI's sixty viewing positions (or rows) were initially affected, the anomaly impact has extended to about 50% of the sensor's viewing positions. As a consequence of the row-anomaly, the global daily coverage attainable during the first four years of operation is no longer possible. Worldwide-coverage is currently achieved in about two-days.

The reduced viewing capability of the sensor may affect the accuracy of the long-term trends of OMI-derived products if the decrease in sampling frequency is so large that the diminished number of observing opportunities does not longer produce statistically equivalent spatial and temporal averages of the measured parameters. Because the OMI sensor still samples the same location every other day, no reduction on the statistical significance of the averaged retrieval results is expected when using different subsets of radiance observations. Statistically non-equivalent results, however, may result if the angular distribution of the scattered and/or reflected incoming radiation is not realistically represented in the retrieval algorithm look-up tables. In version 1.4.2 of the OMAERUV algorithm, all aerosol models are assumed to be poly-dispersions of spherical particles [*Torres et al.*, 2007; 2013] and their scattering phase functions are calculated using Mie Theory. In the UVAI calculation, on the other hand, clouds are modelled as Lambertian opaque surfaces. Prompted by the loss of angular coverage associated with OMI's row anomaly, in this study we carry out a detailed examination of the theoretical treatment of particle scattering in the radiative transfer calculations used in the OMI aerosol algorithm.

In this paper we investigate the effect of the reduced spatial coverage on the representativity of long-term OMI aerosol record by examining the consistency of retrieval results using observation sub-sets associated with different scattering angle ranges. The full OMI viewing capability during the instrument's first three years of operation (2005-2007), allows a comparative analysis of time and space averaged aerosol parameters making use of different subsets of scattering-angle

dependent observations. Section 2 describes in detail the row anomaly affecting the OMI performance followed by a discussion in section 3 of the methodology used in the analysis. Results of the across scan bias analysis conducted over different regions for the quantitative (AOD and SSA) and qualitative (UVAI) products are discussed in sections 4 and 5 respectively, including a discussion of changes in aerosol and cloud model representations required to address the issues identified in this study.

2 Row Anomaly

Anomalous readings consisting on either increase or decrease of radiance signal at individual OMI viewing positions (or rows) started in early 2008. Because the initial manifestation of the problem was limited to individual rows this instrumental issue has been referred to as *'row anomaly'*. Although the exact nature of the problem is not known, it is suspected that the row anomaly is the result of a physical obstruction that developed as a consequence of the loosening of fabric material covering the interior walls of the sensor. Detailed history of row anomaly onset and evolution is contained in lookup tables in the Level 1B software. The OMAERUV algorithm uses the row-anomaly detection method developed for the NASA OMI Total Ozone product (OMTO3) based on statistical analysis. It identifies total ozone anomalies in zonally averaged bands by comparison to data prior to the row anomaly onset [*Schenkeveld et al.*, 2017]. The row anomaly initially affecting two rows in June 2007 has extended to about 50% of the sensor's sixty rows as shown in Fig. 1.

The OMI row anomaly is not static as it slowly evolves over time at both long and short time-scales. It affects the quality of both level 1B spectral radiances and Level 2 products. The first sign of a row anomaly appeared on late June 2007, when a decrease in radiance signal affecting cross-track positions 54 and 55 was observed. Anomalous radiance readings impacting positions 38 through 43 at the northern section of the orbit were detected in May 2008. By December 2008 this effect propagated to position 45 along the entire orbit. Cross-track positions 28 through 45 show signs of degradation depending on orbital position by late January 2009. Since then, the row anomaly has been varying more dynamically, affecting many rows, and occasionally releasing partial rows.

The rate of expansion of the row anomaly has slow down since July 2011. The OMI's KNMI website (http://projects.knmi.nl/omi/research/product/rowanomaly-background.php) provides a more complete description of this instrumental issue.

3 Across Scan Bias Analysis

In this analysis we have made use of the 2005-2007 OMAERUV aerosol record to calculate monthly mean values of derived aerosol parameters over several regions. Viewing positions 1 through 30 on the West of nadir and positions 31 through 60 on the East are separately used. These two sets of observations are hereafter referred to as W and E to facilitate the discussion. Unless the decrease in sampling frequency when using only a subset of the total observations, leads to the no detection of relevant aerosol events, the regional monthly means calculated using different observation sub-sets should be

Atmos. Meas. Tech. Discuss., https://doi.org/10.5194/amt-2017-429
Manuscript under review for journal Atmos. Meas. Tech.
Discussion started: 20 December 2017

statistically equivalent. The retrieved aerosol parameters used in this study are AOD, SSA, and UVAI. Although the study was carried out over several regions, for the sake of brevity, we report results at three regions: Northeast United States (NEUS); Southern Africa (SAF); and the Saharan Desert (SAH). The NEUS region (25N-45N, 60W-90W) representative of areas predominantly associated with non-absorbing aerosols and clouds. SAF (5S-25S, 15E-35E) is a region known as an important source of carbonaceous aerosols, which are often observed mixed with clouds. In the SAH region (SAH, 16N-30N, 30E-10W) desert dust is the most abundant aerosol type, and cloud presence is significantly less than in the other two regions.

Because the across-scan sweep observing mode spans two different ranges of scattering angles, the occurrence of differences between the subsets of analysed data could be associated with the directionally inconsistent characterization of the angular variability of the scattering phase function of aerosols and clouds which is the ultimate driver of the angular distribution of scattered radiation.

4 Effects on AOD and SSA retrievals

4.1 Analysis of results

Figure 2 shows monthly averaged values of retrieved AOD (top panel), and SSA (middle panel) using separately observations on both sides of the scan over the SAF region. The red line depicts the calculated monthly averages using the E subset of observations while the blue line shows those obtained using only the W subset. The bottom panel of Fig. 2 shows the temporal variability of the monthly average scattering angle for each side of the scan. A 140°-165° scattering angle range prevails on the East side while a smaller range (117°-130°) is observed on the West branch of the scan.

The two sets of calculations yield similar results as a function of time, in spite of the different ranges of scattering angles corresponding to the two sets of observations. Largest AOD values and minima SSA values take place in the August-October period when large amounts of absorbing carbonaceous aerosols are known to dominate the atmospheric aerosol load. The close agreement of the W and E retrieved products indicates an adequate representation of the actual aerosol scattering phase function. Similar results, not shown, were obtained over the NEUS region where sulphate aerosols is the most commonly observed aerosol type. The outcome of these comparative analyses suggest that, as expected, the use of Mie Theory for calculating the scattering phase functions of sulphate and carbonaceous aerosols produce consistent representation of the observed angular variability of OMI measured reflectances in spite of the large difference in the scattering angle ranges.

Results of a similar comparison over the Saharan Desert region are shown in Figure 3. Unlike the close agreement between retrievals on both sides of the scan found over the SAF and NEUS regions, large across-scan biases in retrieved AOD are observed over the Saharan region from February through September, when the atmospheric aerosol load is dominated by the presence of typically large dust particles. AOD retrieval differences (top panel) are significant during the February-September period, with largest discrepancies in April-July, which is the time of peak aerosol concentration over this region. On the other hand, during the months of minimum aerosol activity (October through January) AOD retrievals on both sides of the scan are in good agreement with each other at the annual minima AOD values. The seasonality of the observed differences

in SSA retrievals (middle panel) is almost diametrically opposed to that observed in the AOD case. Minima SSA retrieval differences between the two sets of observations are observed during April through August, which are also the months of actual largest AOD as well as lowest SSA. Largest discrepancies between SSA retrievals on both sides of the scan (about 0.02) are observed in the September-March period associated with both lowest aerosol load and highest SSA values. Average values of scattering angles for the West (110°-130°) and East (140°-165°) sides of the scan are shown on the bottom panel of Figure 3.

The scattering-angle-dependent results of retrieved aerosol optical depth and single scattering albedo over the Saharan Desert suggests an inadequate model representation of the scattering properties of desert dust particles assumed to be spherically shaped in the OMAERUV algorithm. Desert dust aerosols are known to be irregularly shaped large particles whose phase function may deviate significantly from that of a spherical model at scattering angles larger than about 80° for non-absorbing particles. The role of particle shape assumption in the retrieval of desert dust properties was recently identified as an important source of uncertainty in the OMAERUV algorithm [*Gassó and Torres,* 2016]. An analysis of the uncertainty in retrieved AOD and SSA associated with the spherical shape assumption of desert dust particles is presented next.

4.2 Sensitivity Analysis

Accurate representation of the scattering phase function of large nonspherical particles requires the use of adequate analytical tools such as T-matrix theory [*Waterman,* 1971; *Bohren and Singham,* 1991; *Mishchenko and Travis,* 1994], geometric optics [*Yang and Liou,* 1996] or a combination of the two approaches [*Dubovik et al,* 2006]. The simplest non-spherical shapes for which exact analytical solutions can be obtained are spheroids whose shapes are characterized by their aspect or axis ratio. Although it has been shown that the spheroid assumption using T-matrix theory reproduce laboratory measurements of the scattering phase function significantly better than spheres, it breaks down for highly elongated and flattened spheroids [*Mishchenko et al.,* 2002] of very large size parameter ($2\pi r/\lambda$). The Geometric Optics method documented by *Yang and Liou* [2000] accurately accounts for scattering effects of spheroids of aspects ratios and size parameters beyond T-matrix capabilities. *Dubovik et al.* [2006] combined the advantages of the T-matrix and Geometric Optics to create a set of look-up tables of phase matrix elements for aspects ratios in the range 0.3 to 3.0 and size parameters from 0.012 to 625. In the following analysis we used the *Dubovik et al.* [2006] kernels and the associated software package available from the author.

Retrieval errors associated with aerosol particles non-sphericity in the near UV were analysed in the context of volcanic ash detection and characterization [*Krotkov et al.,* 1999]. In this section we carry out a sensitivity analysis to evaluate the effect of ignoring aerosol non-sphericity in the retrieval of AOD and SSA of desert dust aerosols by the OMAERUV algorithm. Scattering matrix elements extracted from the *Dubovik et al.* [2006] kernel package were fed to a vector radiative transfer code to generate top-of-the-atmosphere (TOA) radiances at 354 and 388 nm for an atmosphere containing a polydispersion of non-spherical particles. The calculated radiances, associated with specific AOD and SSA values were used as input to a research version of the OMAERUV algorithm that assumes desert dust to be spherical particles. Except for the scattering phase function,

all other aerosol properties, i.e., particle size distribution and refractive index are identical to those of the standard OMAERUV desert dust models [*Torres et al.*, 2007].

Figure 4 (top) illustrates simulated AOD retrieval errors (in percent) as a function of scattering angle when non-spherical aerosol models of varying single scattering albedo are treated as spherical particles in the inversion procedure. The vertical lines indicate the range of average scattering angle associated with the West (red lines) and East (blue lines) sections of the scan as shown on the bottom panel of Figure 3. Retrieval errors transition from overestimations to underestimations at about 155° scattering angle.

On the 110°-130 scattering angle range, associated with OMI's average viewing geometry on the West side of the scan, AOD errors are always positive, and show little angular dependence. Retrieval errors vary between about 13% for the model of lowest SSA value used in the analysis (0.83) and close to 23% for the least absorbing case (SSA = 0.97). For the range of average scattering angles (140°-165°) corresponding to the East side of OMI's scan, positive AOD retrieval errors decrease rapidly with scattering angle. Much larger underestimation errors take place for scattering angles larger than 155°, with the error rapidly increasing with scattering angle. For weakly absorbing aerosols, errors in excess of 100% are possible at scattering angles larger than 165°. Because the inversion algorithm simultaneously retrieves both AOD and SSA, no AOD is retrieved in cases when the retrieved SSA is unphysical as discussed next.

Absolute errors in retrieved SSA associated with the spherical shape assumption for the same set of aerosol models in the previous discussion are shown on the bottom panel of Fig. 4. Small negative and positive errors (absolute value less than 0.01) take place for scattering angles smaller than 160°. For aerosols of actual SSA larger than about 0.92, the retrieved value is slightly overestimated whereas for more absorbing particles a small SSA underestimation takes place. The error increases with decreasing SSA and is largest (about -0.01) for the aerosol model of lowest modelled SSA (0.83). At scattering angles larger than 160°, SSA retrievals are underestimated for aerosol models of SSA smaller than 0.9 with errors as large as 0.02 at 165° scattering angle and even larger in the near backscatter direction.

The previous sensitivity analysis allows the interpretation of the observed W-E differences in retrieved AOD and SSA depicted in Figure 3. According to these results, retrieved AOD values on the West side of the scan, where the average scattering angle stays in the range 110°-130°, are overestimated whereas those on the East side are underestimated. Because the average scattering angle on the East branch of the scan remains above 160° from March through September, the resulting AOD is underestimated. It can also be inferred that the magnitude of the underestimation is much larger than that of the overestimation which explains the large difference in W-E dust AOD retrievals in Figure 3. Regarding the SSA retrieval, the observed W-E differences (as large as 0.02 but within 0.01 most of the time) in retrieved SSA are consistent with the results of the sensitivity analysis that indicates that, in addition to the angular dependence, the magnitude of the retrieval error also depends on the actual SSA value.

4.3 Application to OMI observations

Atmos. Meas. Tech. Discuss., https://doi.org/10.5194/amt-2017-429
Manuscript under review for journal Atmos. Meas. Tech.
Discussion started: 20 December 2017

A new set of look-up tables at 354 and 388 nm calculated for the spheroidal particle shape model described in section 4.2 were used in a research version of the OMAERUV inversion algorithm. Retrieval results are shown in Figure 5. The resulting W-E AOD scan bias was reduced from values as high as 0.25 in June 2006 (Fig. 3) to about 0.02 (Fig. 5). The amplitude of the across-scan SSA bias (middle panel) was reduced from about 0.025 to 0.015. However, a small bias of about 0.007 is still present. Because of cancellation of small remaining biases in AOD and SSA, the calculated AAOD W-E differences are smaller than 0.005 (bottom panel).

As shown in Fig. 5, accounting for the non-sphericity of aerosol particles virtually eliminates the large across-scan AOD bias observed when the spherical particle shape approximation is used. The non-spherical shape approximation reduces further the small error SSA error associated with the spherical particle shape assumption.

5 UV Aerosol Index

5.1 Scan bias Analysis

The UVAI calculated as shown in Appendix A, is a residual parameter that quantifies the difference between measured and calculated ratios of UV radiances [*Torres et al.*, 1998]. When all radiative transfer processes are effectively accounted for, the UVAI should, by definition, be zero. Unlike with the retrieval of quantitative aerosol parameters that require cloud screening, the UVAI is calculated for all observations regardless of cloudiness conditions or ice/snow presence.

In this section, we examine the directional consistency of the UVAI parameter in a manner similar to that in the previous section. Figure 6 (top panel) depicts monthly mean UVAI over the NEUS region calculated separately for the West and East sections of the scan. Near-zero W-E differences are observed in February followed by a rapid increase to a maximum of about 0.4 from May through July when it starts to decrease again to near-zero difference in October. A similar situation, observed over the SAF region, is depicted in the center panel of Figure 6. Here, the absolute W-E differences are largest in January (about 0.5), decrease to zero by May and remain low until August, when the two average values start diverging again. The time series of UVAI is also shown for the SAH region in the bottom panel of Figure 6. Largest W-E differences of about 0.2 UVAI units are observed during the spring months.

There is a clear contrast between the small W-E differences in the SAH region and the much larger ones over the other two regions in Fig. 6. The most relevant difference between the SAH region and the NEUS and SAF regions is the significantly reduced levels of cloudiness in the former. Thus, the much smaller UVAI across-scan bias over the SAH region where cloudiness is generally very low during the entire year, and the observed season dependent angular bias over the NEUS and SAF regions, suggest that the angular dependence of cloud scattering effects may not have been adequately accounted for in the UVAI calculation. A more detailed visualization of the cross-track angular dependence of the UVAI over the NEUS region in January and July 2005 is shown in Figure 7. In the next section we will examine if the observed W-E differences reported here can be explained by the way cloud reflection effects are treated in the UVAI computation.

Atmos. Meas. Tech. Discuss., https://doi.org/10.5194/amt-2017-429
Manuscript under review for journal Atmos. Meas. Tech.
Discussion started: 20 December 2017

5.2 Parameterization of cloud effects in UVAI calculation

The UVAI in the OMAERUV algorithm is currently calculated using the SLER approximation described in Appendix A. In this approach the combined effect of surface and cloud reflection, as well as scattering and absorption aerosol effects is represented by an opaque Lambertian reflector located at the surface. In the presence of clouds, therefore, the SLER representation does not capture the angular variability associated with the scattering phase function of clouds. Such an approximation may, therefore, be responsible for the across-scan UVAI bias observed by the OMI sensor as discussed in section 4. To test that hypothesis, we have developed an alternate way of calculating the UVAI that explicitly accounts for scattering effects of water clouds following the results of a previous study showing that the use of Mie scattering theory reproduces remarkably well the satellite observed field of backscattered UV radiation in a cloudy atmosphere [*Ahmad et al.*, 2004]. In this approach, it is assumed that the radiance measured by the sensor at pixel level emanates from a combination of clear and cloudy conditions (I_λ^s and I_λ^C) involving a cloud of fixed optical depth and varying cloud fraction. The I_λ^s terms are calculated using wavelength dependent climatological values of surface albedo, derived from analysis of the 10-year long-term OMI record of minimum reflectivity. The I_λ^C terms, on the other hand, are calculated using Mie scattering theory for an assumed water cloud model [*Deirmendjian,* 1964] and wavelength-dependent refractive index [*Hale and Querry*, 1973], at prescribed top and bottom levels, and fixed cloud optical depth (COD). The choice of COD value (10) is based on the highest frequency of occurrence of this value reported by MODIS observations [*King et al.,* 2013]. A wavelength independent geometric cloud fraction, f_g, is calculated from equation

$$f_g = \frac{I_{\lambda_0}^{obs} - I_{\lambda_0}^s}{I_{\lambda_0}^C - I_{\lambda_0}^s} \quad (1).$$

When the resulting cloud fraction is larger than unity, overcast sky conditions are assumed (i.e., f_g=*1.0*), and a new I_λ^C term for COD value larger than 10 that matches $I_{\lambda_0}^{obs}$ is derived. I_λ^{cal} values are then obtained from equation,

$$I_\lambda^{cal} = (1.0 - f_g) I_\lambda^s + f I_\lambda^C \quad (2),$$

and used as input in the calculation of the UVAI in equation A-1.

This way of calculating the I_λ^{cal} term is conceptually similar to the MLER method [*McPeters et al, 1998; Penning De Vries and Wagner*, 2011] described in Appendix A. The major difference is that while in the MLER approach clouds are modelled as Lambertian opaque surfaces using Rayleigh scattering calculations, the method tested here treats clouds as polydispersions of liquid water droplets, and uses Mie radiative transfer theory in the forward calculations.

5.3 Evaluation of Results

Figure 8 depicts the resulting cross-track angular dependence of the UVAI over the NEUS region in January and July 2005 when applying the Mie-based approach. For both months, the resulting angular dependence is significantly reduced in relation to that shown in Figure 7 when using the SLER-based method of UVAI calculation. Largest improvements are observed for positions 1 through 20 associated with scattering angle ranges 80-110 for January and 100-140 for July. Overall, the Mie UVAI is closer to zero at all angular positions yielding very small W-E differences as shown in Fig 9. The better performance of the Mie-based approach is consistent with the results of *Ahmad et al.* [2004] who found out that Mie radiative transfer calculations using the C1 cloud model reproduced satellite observed UV radiances over a large range of viewing conditions better than parameterizations that model clouds as opaque surfaces.

Figure 9 shows the comparison of resulting across-scan bias in UVAI calculated using the Mie-based definition tested here. The W-E biases observed using the standard SLER UVAI definition application in Figure 6, have been reduced in the three regions used in the analysis. Significant cross-track bias reduction is observed over the NEUS and SAF regions where high cloudiness levels prevail.

A global comparison of resulting Mie and SLER based UVAI definitions under cloudy conditions are shown in Fig. 10 for August 20, 2007. The across-scan bias of the Mie-based UVAI map, shown on the middle panel, is significantly reduced in relation to the corresponding SLER-based UVAI map depicted in the top panel. To facilitate the comparison, the bottom panel of Fig 10 shows the associated reflectivity field. A clear reduction in across-scan Mie UVAI bias is observed over cloudy regions of reflectivity larger than about 20%.

6 Summary and conclusions

An analysis of the effect of OMI's reduced viewing capability on the representativity of time and space averaged aerosol products has been carried out. Regional monthly average values of AOD, SSA and UVAI, retrieved from observations using two different set scattering angles associated with off-nadir viewing geometries on the East and on the West of nadir were compared. Close agreement between the two sets of averaged retrieval results was expected under the assumption that the forward-model-calculated angular dependence of the radiation field in the presence of aerosols and clouds realistically reproduces the actual angular scattering patterns of cloud and aerosol particles.

The expected agreement in the retrieved AOD and SSA properties was obtained in cases where the aerosol load consisted of either carbonaceous or sulphate aerosols, known to be predominantly small spherical particles, and whose scattering phase function is calculated using Mie scattering theory. Large differences in retrieved AOD values, however, were found for retrieval conditions when the aerosol load was mainly desert dust, made up of predominantly large non-spherical particles. Small errors in retrieved dust SSA were also found. Because the retrieval algorithm also makes use of Mie Theory to calculate the scattering properties of desert dust aerosols, the wrong particle shape assumption appeared to be the likely source of the discrepancy. The analysis was then repeated using a research version of the retrieval algorithm in which the scattering properties of desert dust aerosols were obtained using a combination of T-matrix and geometric optics calculations.

The observed differences between the two retrievals under the spherical shape assumption reduced significantly when using the non-spherical particle shape approximation.

Differences between the two sets of observations were also observed in the retrieved UVAI over the NEUS and SAF regions were clouds are persistently present. No significant differences were observed under the predominantly cloud free conditions prevailing over the SAH region. The source of the difference turned out to be the currently used parameterization of cloud scattering effects in the calculation of UVAI in which clouds are treated as opaque Lambertian reflectors located at the surface. In the presence of clouds, this representation does not capture the angular variability associated with the scattering effect of clouds. A modified version of the UVAI algorithm in which a more physically based approach is used to incorporate cloud scattering of incoming radiation was developed and tested. Obtained results largely eliminated the observed differences between the two sets of observations.

The analysis discussed here has uncovered important algorithmic deficiencies associated with the model representation of the angular dependence of scattering effects of desert dust aerosols and cloud droplets. The resulting improvements in the handling of desert dust and cloud scattering have been incorporated in a revised version of the OMAERUV algorithm. With these modifications, OMAERUV retrievals can be used for trend analyses in spite of the reduction of about 50% in the sensor's viewing capability.

Acknowledgements

This work was carried out under the auspices of a NASA Aura ROSES proposal, NNH13ZDA001N-AURA, Ken Jucks (program manager).

References

Acarreta, J. R., De Haan, J. F., and Stammes, P.: Cloud pressure retrieval using the O2-O2 absorption band at 477 nm, J. Geophys.Res., 109, D05204, doi:10.1029/2003JD003915, 2004.

Ahmad, Z., P. K. Bhartia, *and* N. Krotkov *(*2004*),* Spectral properties of backscattered UV radiation in cloudy atmospheres, *J. Geophys. Res.*, 109, *D01201*, *doi:*10.1029/2003JD003395.

Ahn, C., O. Torres, *and* H. Jethva *(*2014*),* Assessment of OMI near-UV aerosol optical depth over land, *J. Geophys. Res. Atmos.*, 119, 2457–2473, *doi:*10.1002/2013JD020188.

Ahn C., O. Torres, and P.K. Bhartia, Comparison of OMI UV Aerosol Products with Aqua-MODIS and MISR observations in 2006, *J. Geophys. Res*, 113, D16S27, doi:10.1029/2007JD008832, 2008

Boersma, K. F., Eskes, H. J., Dirksen, R. J., van der A, R. J., Veefkind, J. P., Stammes, P., Huijnen, V., Kleipool, Q. L., Sneep, M., Claas, J., Leitão, J., Richter, A., Zhou, Y., and Brunner, D.: An improved tropospheric NO_2 column retrieval algorithm for the Ozone Monitoring Instrument, Atmos. Meas. Tech., 4, 1905–1928, doi:10.5194/amt-4-1905-2011, 2011.

Bohren, C. F., and S. B. Singham (1991), Backscattering by nonspherical particles: A review of methods and suggested new approaches, *J. Geophys. Res.*, 96, 5269–5277.

Deirmendjian, D., Scattering and polarization properties of water clouds and hazes in the visible and infrared, *Appl. Opt*., 3, 187-196, 1964.

Dubovik, O., *et al. (*2006*),* Application of spheroid models to account for aerosol particle nonsphericity in remote sensing of desert dust, *J. Geophys. Res.*, 111, *D11208*, *doi:*10.1029/2005JD006619.

Gassó, S. and O. Torres (2016), The role of cloud contamination, aerosol layer height and aerosol model in the assessment of the OMI near-UV retrievals over the ocean, *Atmos. Meas. Tech*., 9, 3031-3052, doi:10.5194/amt-9-3031-2016, 2016.

González Abad, G., Liu, X., Chance, K., Wang, H., Kurosu, T. P., and Suleiman, R.: Updated Smithsonian Astrophysical Observatory Ozone Monitoring Instrument (SAO OMI) formaldehyde retrieval, Atmos. Meas. Tech., 8, 19-32, https://doi.org/10.5194/amt-8-19-2015, 2015.

Hale G. and M. Querry, (1973), Optical Constants of Water in the 200-nm to 200-µm Wavelength Region, *Appl. Opt.* 12, 555-563.

Jethva, H., O. Torres, and C. Ahn (2014), Global assessment of OMI aerosol single-scattering albedo using ground-based AERONET inversion, *J. Geophys. Res. Atmos.*, 119, doi:10.1002/2014JD021672.

Joiner, J., and A. P. Vasilkov (2006), First results from the OMI rotational-Raman scattering cloud pressure algorithm, *IEEE Trans. Geosci. Remote Sens.* 44, 1272–1282, doi:10.1109/TGRS.2005.861385.

King, M. D., Platnick, S., Menzel, W. P., Ackerman, S. A., and Hubanks, P. A.: Spatial and Temporal Distribution of Clouds Observed by MODIS Onboard the Terra and Aqua Satellites, *IEEE T. Geosci. Remote*, 51, 3826–3852, doi:10.1109/TGRS.2012.2227333, 2013.

Krotkov, N. A., McLinden, C. A., Li, C., Lamsal, L. N., Celarier, E. A., Marchenko, S. V., Swartz, W. H., Bucsela, E. J., Joiner, J., Duncan, B. N., Boersma, K. F., Veefkind, J. P., Levelt, P. F., Fioletov, V. E., Dickerson, R. R., He, H., Lu, Z., and Streets, D. G.: Aura OMI observations of regional SO_2 and NO_2 pollution changes from 2005 to 2015, Atmos. Chem. Phys., 16, 4605-4629, https://doi.org/10.5194/acp-16-4605-2016, 2016.

Kroktov, N.A., D.E. Flittner, A.J. Krueger, A Kostinski, C. Riley, W. Rose and O. Torres (1999), Effect of particle non-sphericiy on satellite monitoring of drifting volcanic clouds, *J. Quant. Spectrosc. Radiat. Tansfer*, 63, 613-630.

Levelt, P.F., E. Hilsenrath, G.W. Leppelmeier, G.H.J. van den Ooord, P.K. Bhartia, J. Taminnen, J.F. de Haan, and J.P. Veefkind, Science Objectives of the Ozone Monitoring Instrument, *IEEE Trans. Geo. Rem. Sens,*. Special Issue of the EOS-Aura mission, 44(5), 1093-1101, 2006

Li, C., J. Joiner, N. A. Krotkov, and P. K. Bhartia (2013), A fast and sensitive new satellite SO_2 retrieval algorithm based on principal component analysis: Application to the Ozone Monitoring Instrument, Geophys. Res. Lett., 40, 6314–6318, doi:10.1002/2013GL058134.

Livingston, J. M., J. Redemann, P. B. Russell, O. Torres, B. Veihelmann, P. Veefkind, R. Braak, A. Smirnov, L. Remer, R. W. Bergstrom, O. Coddington, K. S. Schmidt, P. Pilewskie, R. Johnson, and Q. Zhang (2009), Comparison of aerosol optical depths from the Ozone Monitoring Instrument (OMI) on Aura with results from airborne sunphotometry, other space and ground measurements during MILAGRO/INTEX-B, Atmos. Chem. Phys., 9, 6743–6765

McPeters, R. D., Bhartia, P. K., Krueger, A. J., Herman, J. R., Wellemeyer, C. G., Seftor, C. J., Jaross, G., Torres, O., Moy, L., Labow, G., Byerly, W., Taylor, S. L., Swissler, T., and Cebula, R. P.: Earth Probe Total Ozone Mapping Spectrometer (TOMS) Data Products User's Guide, NASA Technical Publication 1998-206895, 1998.

McPeters, R. D., Frith, S., and Labow, G. J.: OMI total column ozone: extending the long-term data record, Atmos. Meas. Tech., 8, 4845-4850, https://doi.org/10.5194/amt-8-4845-2015, 2015.

Mishchenko, M. I., and L. D. Travis (1994), T-matrix computations of light scattering by large spheroidal particles, Opt. Commun., 109, 16–21.

Mishchenko, M. I., A. A. Lacis, B. E. Carlson, and L. D. Travis (1995), Nonsphericity of dust-like aerosols: Implications for aerosol remote sensing and climate modeling, *Geophys. Res. Lett.*, 22, 1077– 1080.

Penning de Vries, M. and Wagner, T.: Modelled and measured effects of clouds on UV Aerosol Indices on a local, regional, and global scale, Atmos. Chem. Phys., 11, 12715-12735, doi:10.5194/acp-11-12715-2011, 2011.

Schenkeveld, V. M. E., Jaross, G., Marchenko, S., Haffner, D., Kleipool, Q. L., Rozemeijer, N. C., Veefkind, J. P., and Levelt, P. F., In-flight performance of the Ozone Monitoring Instrument, Atmos. Meas. Tech., 10, 1957-1986, https://doi.org/10.5194/amt-10-1957-2017, 2017.

Torres O., P.K. Bhartia, J.R. Herman and Z. Ahmad, Derivation of aerosol properties from satellite measurements of backscattered ultraviolet radiation. Theoretical Basis, *J. Geophys. Res.*, 103, 17099-17110, 1998

Torres, O., A. Tanskanen, B. Veihelman, C. Ahn, R. Braak, P. K. Bhartia, P. Veefkind, and P. Levelt, Aerosols and Surface UV Products from OMI Observations: An Overview, *J. Geophys. Res.*, 112, D24S47, doi:10.1029/2007JD008809, 2007

Torres, O., Ahn, C., and Chen, Z.: Improvements to the OMI near UV aerosol algorithm using A-train CALIOP and AIRS observations, *Atmos. Meas. Tech.*, 6, 5621-5652, doi:10.5194/amtd-6-5621-2013, 2013.

Waterman, P. C., Symmetry, unitarity, and geometry in electromagnetic scattering, Phys. Rev., D3, 825-839, 1971.

Yang, P., and K. N. Liou (1996), Geometric-optics-integral-equation method for light scattering by nonspherical ice crystals, *Appl. Opt.*, 35, 6568–6584.

Yang, P., K. N. Liou, M. I. Mishchenko, and B. C. Gao (2000), Efficient finite-difference time-domain scheme for light scattering by dielectric particles: Application to aerosols, *Appl. Opt.*, 39, 3727– 3737.

Zhang, W., X. Gu, H. Xu, T. Yu, *and* F. Zheng *(*2016*),* Assessment of OMI near-UV aerosol optical depth over Central and East Asia, *J. Geophys. Res. Atmos.*, 121, 382–398, *doi:*10.1002/2015JD024103.

Atmos. Meas. Tech. Discuss., https://doi.org/10.5194/amt-2017-429
Manuscript under review for journal Atmos. Meas. Tech.
Discussion started: 20 December 2017

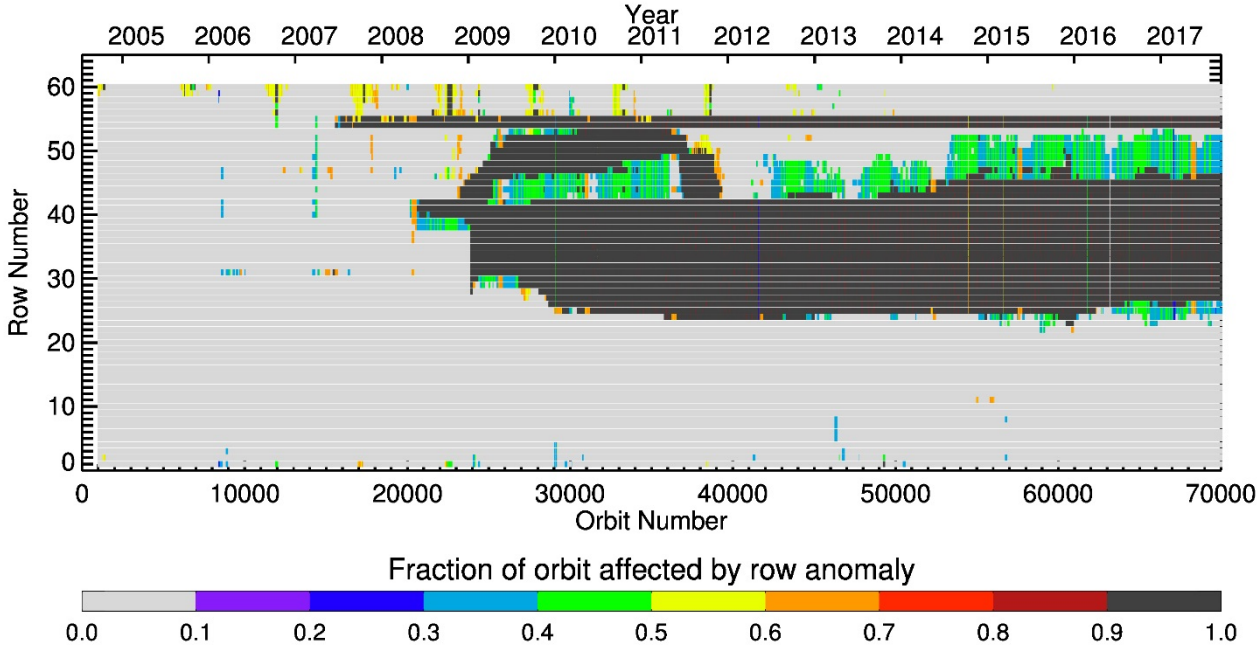

Figure 1. Temporal evolution of the row anomaly as a function of orbit number (bottom) and year (top). The color scale indicates the fraction of orbit impacted by the anomaly.

Atmos. Meas. Tech. Discuss., https://doi.org/10.5194/amt-2017-429
Manuscript under review for journal Atmos. Meas. Tech.
Discussion started: 20 December 2017

Atmospheric Measurement Techniques Discussions

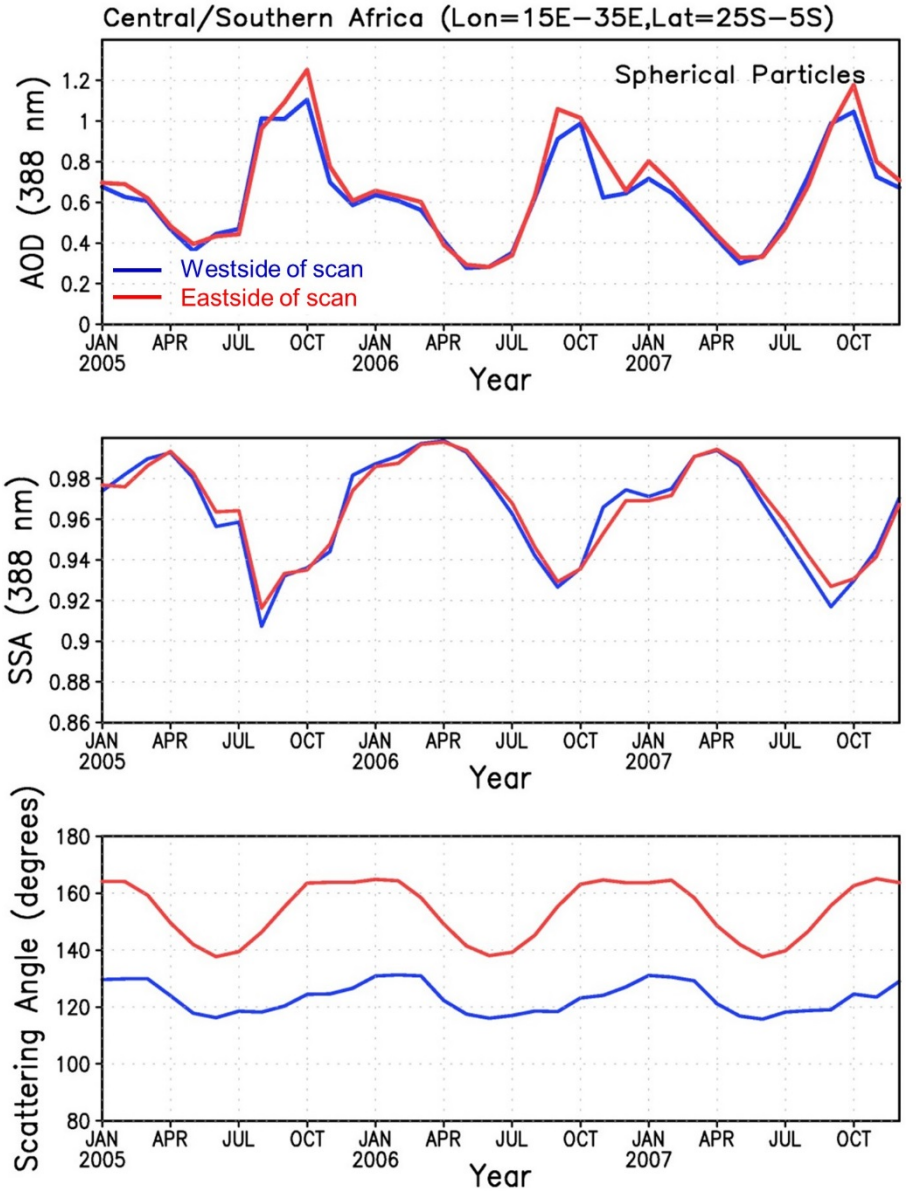

Figure 2. Time series of monthly averages of OMI retrieved AOD (top panel) and SSA (middle panel) over Southern Africa. The red line represents the average calculated from observations by rows 1 through 30 whereas the blue line indicate the resulting averages when using rows 31 through 60. The bottom panel shows the average scattering angle for the two data subsets. See text for details.

Atmos. Meas. Tech. Discuss., https://doi.org/10.5194/amt-2017-429
Manuscript under review for journal Atmos. Meas. Tech.
Discussion started: 20 December 2017

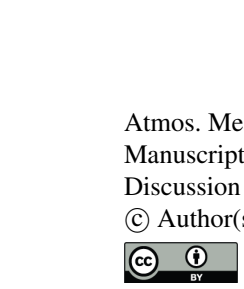

Atmospheric Measurement Techniques Discussions

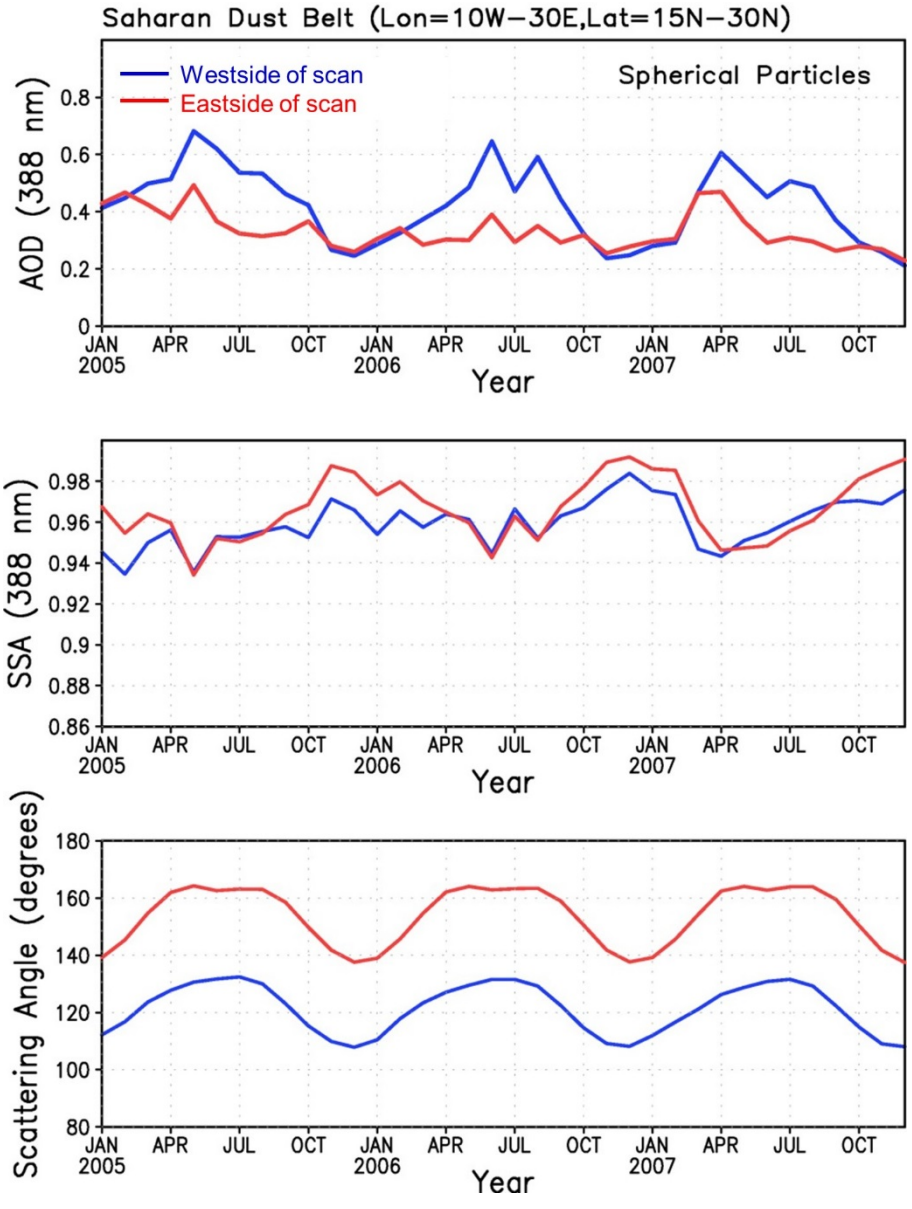

Figure 3. As in Fig. 2 for the Saharan desert region.

Atmos. Meas. Tech. Discuss., https://doi.org/10.5194/amt-2017-429
Manuscript under review for journal Atmos. Meas. Tech.
Discussion started: 20 December 2017

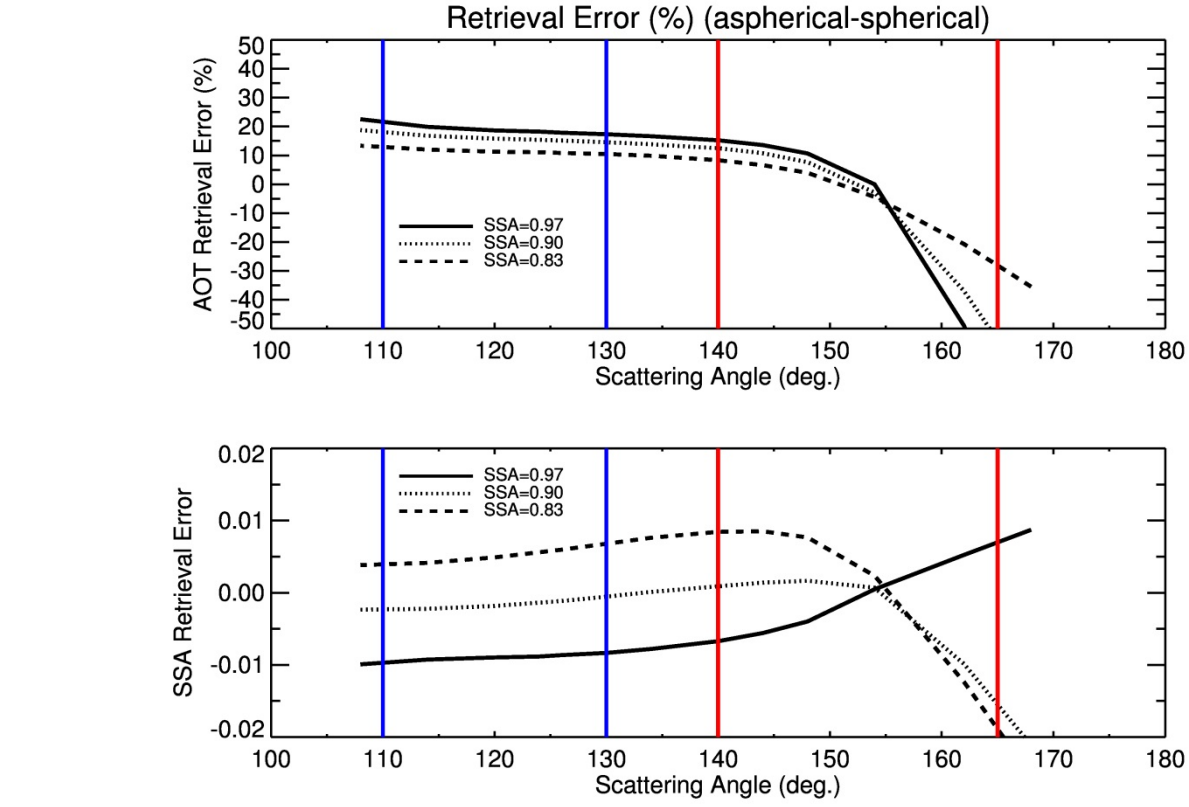

Figure 4. Percent error in retrieved AOD (top) for a non-spherical aerosol polydispersion of optical depth 1.0 (500 nm) assumed to be spherical in the retrieval process. Calculations were done for different SSA values: 0.97 (solid line), 0.90 (dotted line), and 0.83 (dashed line). Vertical lines indicate the range of scattering angles in Fig. 3 for rows 1-30 (blue) and rows 31-60 (red). The bottom panel shows the resulting absolute error in retrieved SSA associated with the spherical particle assumption. See text for details.

Atmos. Meas. Tech. Discuss., https://doi.org/10.5194/amt-2017-429
Manuscript under review for journal Atmos. Meas. Tech.
Discussion started: 20 December 2017

Atmospheric Measurement Techniques Discussions

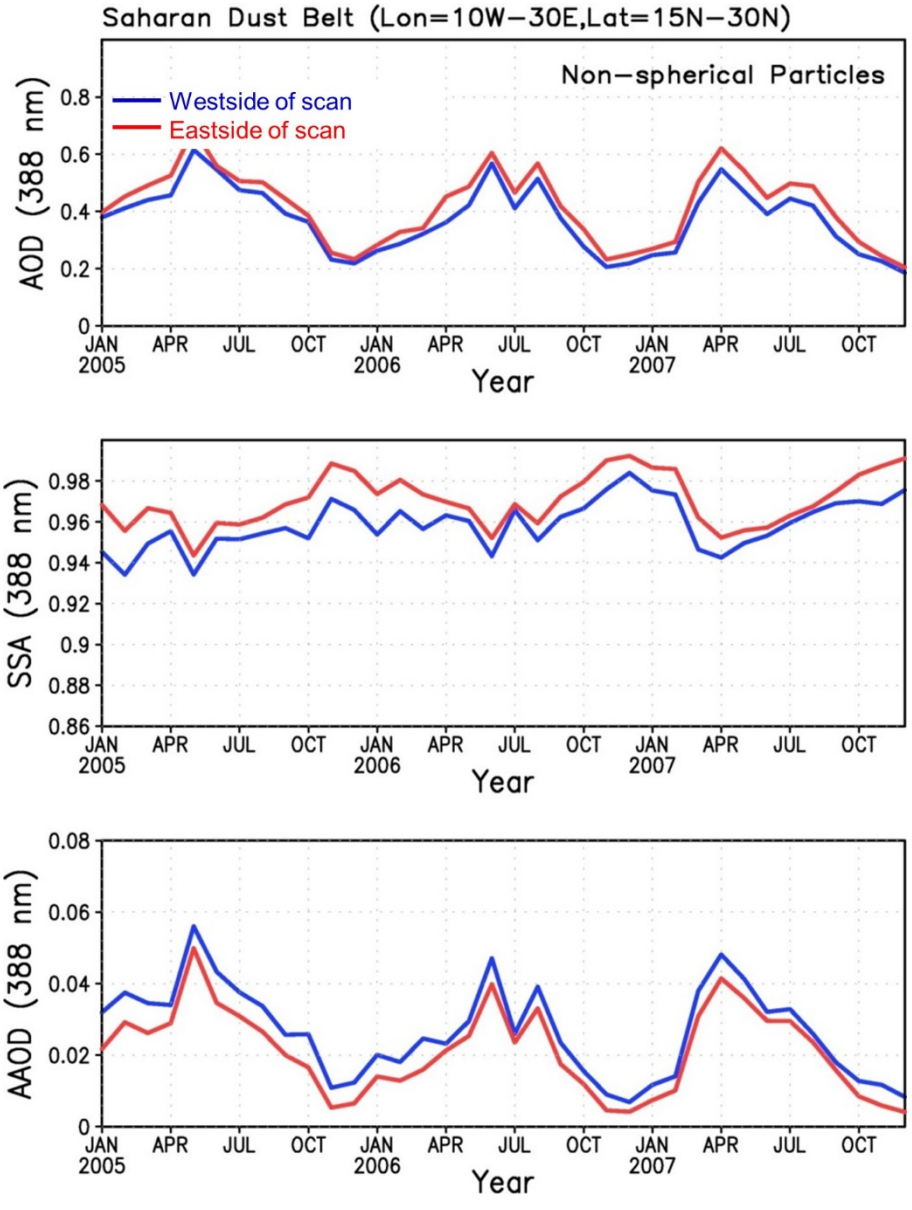

Figure 5. Time series of monthly averages of retrieved AOD (top panel), SSA (middle panel), and AAOD (bottom panel) over the Saharan Desert. Retrievals carried out using an OMI research algorithm that accounts for aerosol non-sphericity. Line color interpretation same as in Figure 3.

Atmos. Meas. Tech. Discuss., https://doi.org/10.5194/amt-2017-429
Manuscript under review for journal Atmos. Meas. Tech.
Discussion started: 20 December 2017

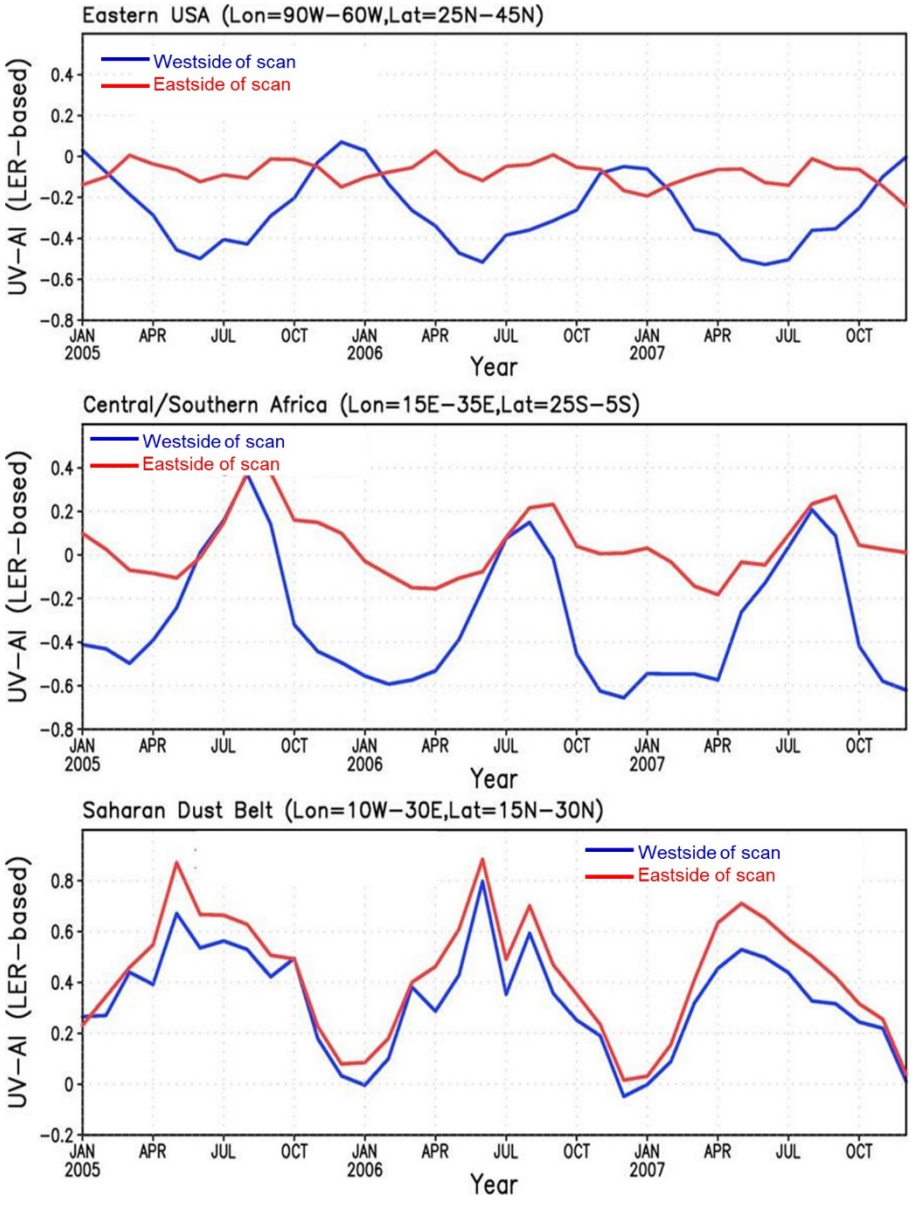

Figure 6. Time series of calculated monthly average UV-AI over the Northeast US (top), SAF (middle), and SAH (bottom) regions using rows 1 to 30 (blue) and 31 to 60 (red).

Atmos. Meas. Tech. Discuss., https://doi.org/10.5194/amt-2017-429
Manuscript under review for journal Atmos. Meas. Tech.
Discussion started: 20 December 2017

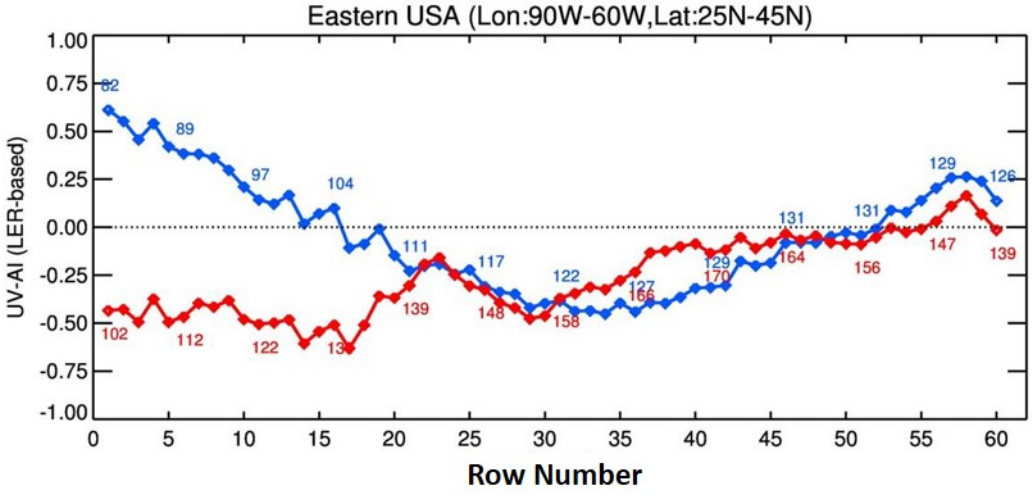

Figure 7. Monthly average values of retrieved LER-based UVAI as a function of viewing position (or row) number. Results for January (blue) and July (red) 2005 are shown. Numbers indicate the monthly average scattering angle for each row.

Atmos. Meas. Tech. Discuss., https://doi.org/10.5194/amt-2017-429
Manuscript under review for journal Atmos. Meas. Tech.
Discussion started: 20 December 2017

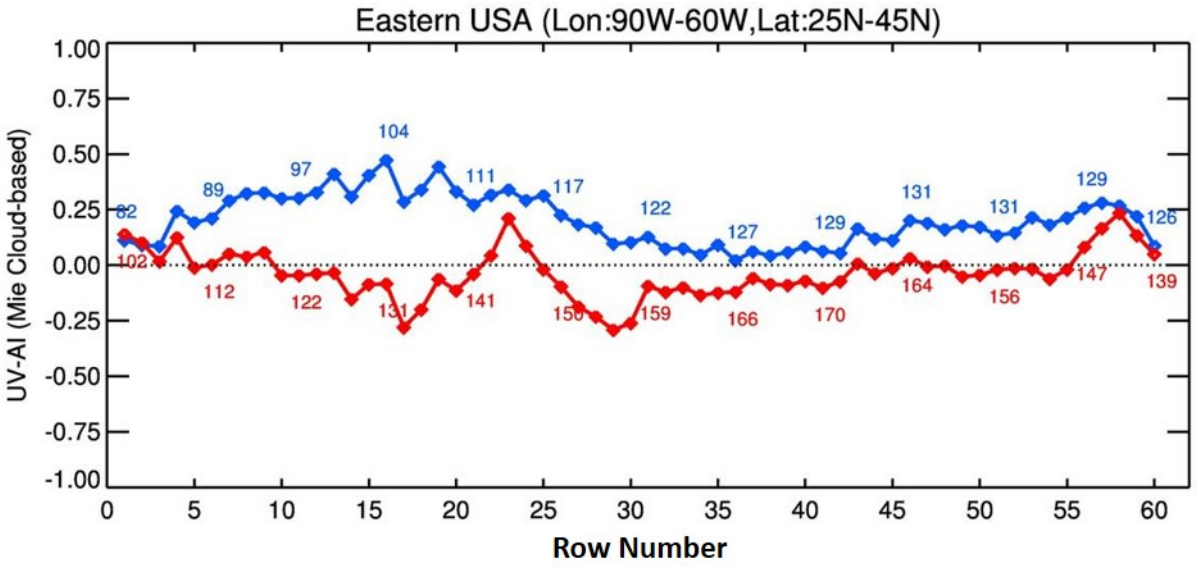

Figure 8. As in Fig. 7 for UVAI calculated with a modified algorithm that explicitly accounts for cloud scattering effects.

Atmos. Meas. Tech. Discuss., https://doi.org/10.5194/amt-2017-429
Manuscript under review for journal Atmos. Meas. Tech.
Discussion started: 20 December 2017

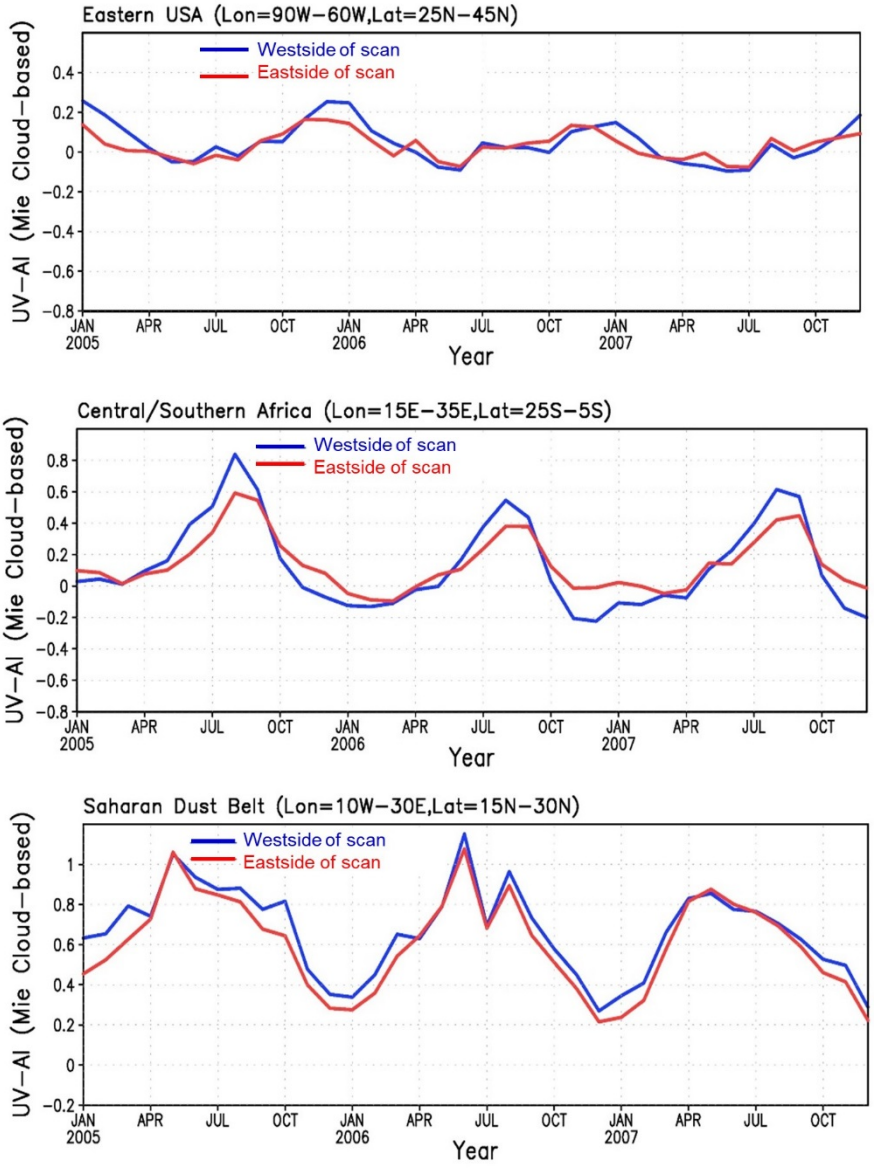

Figure 9. As in Fig. 6 using the Mie UVAI definition.

Atmos. Meas. Tech. Discuss., https://doi.org/10.5194/amt-2017-429
Manuscript under review for journal Atmos. Meas. Tech.
Discussion started: 20 December 2017

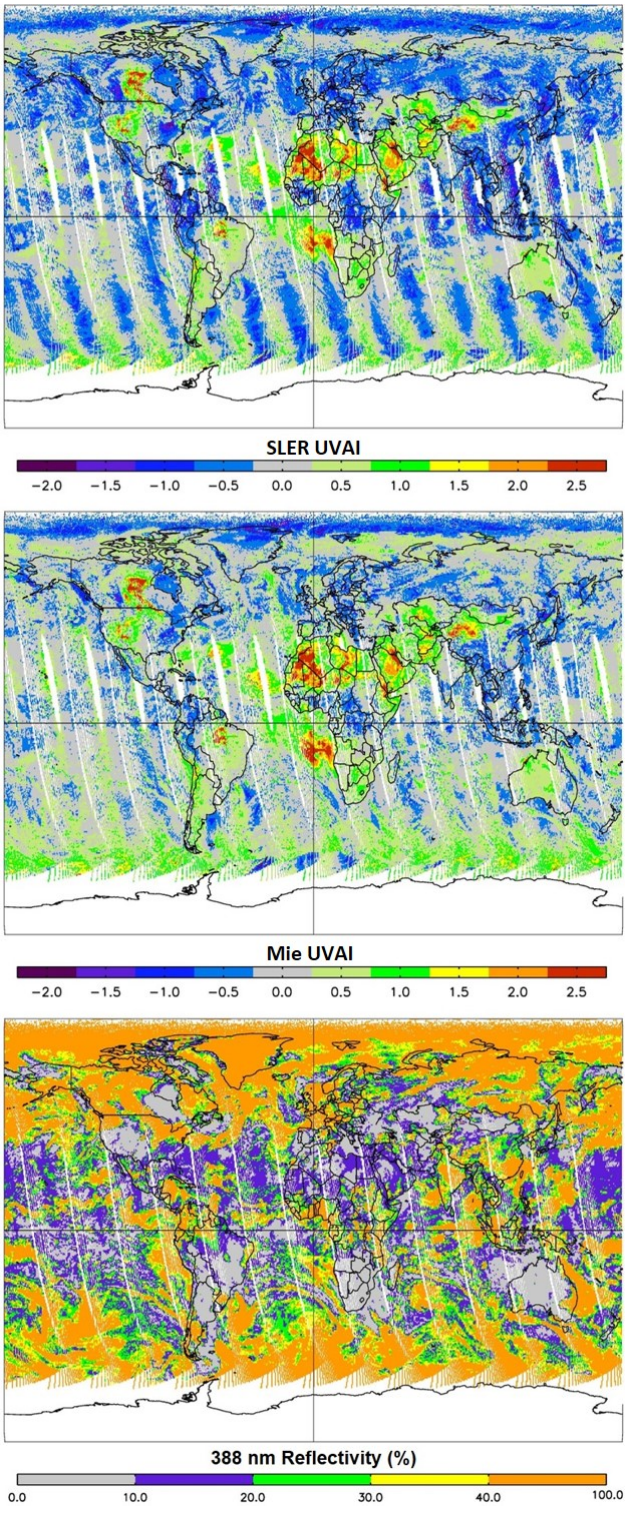

Fig. 10. Global depiction of SLER AAI, Mie UVAI and scene reflectivity on August 20, 2007.

Atmos. Meas. Tech. Discuss., https://doi.org/10.5194/amt-2017-429
Manuscript under review for journal Atmos. Meas. Tech.
Discussion started: 20 December 2017

Atmospheric Measurement Techniques Discussions

Appendix A

UV Aerosol Index Calculation

The UVAI is defined as the difference between the logarithms of the ratio of observed and calculated radiances *(I)* at two near UV wavelengths, λ and λ_0

$$UVAI = -100\left\{\log_{10}\left[\frac{I_{\lambda}^{obs}}{I_{\lambda_0}^{obs}}\right] - \log\left[\frac{I_{\lambda}^{cal}}{I_{\lambda_0}^{cal}}\right]\right\} = -100\log_{10}\left[\frac{I_{\lambda}^{obs}}{I_{\lambda}^{cal}}\right] \quad \text{(A-1)}$$

λ_0 (generally longer than λ) represents the wavelength at which the scene Lambertian reflectivity R is calculated using the expression

$$R_{\lambda_0} = \frac{I_{\lambda_0}^{obs} - I_{\lambda_0}^{0}}{T_{\lambda_0} + S_{\lambda_0}(I_{\lambda_0}^{obs} - I_{\lambda_0}^{0})} \quad \text{(A-2)}$$

where $I_{\lambda_0}^{0}$ is the path radiance, T_{λ_0} is the two-way transmittance, and S_{λ_0} is the spherical albedo for illumination from below of a purely molecular atmosphere.

A.1 Simple Lambertian Equivalent Reflector (SLER) approximation

By definition, at λ_0 the terms I^{cal} and I^{obs} are mathematically identical. The calculated radiance I_{λ}^{cal}, is found by using the calculated R in the Lambertian approximation of the radiative transfer equation under the assumption that R is wavelength independent,

$$I_{\lambda}^{cal} = I_{\lambda}^{0} + \frac{RT_{\lambda}}{1 - R\,S_{\lambda}} \quad \text{(A-3)}$$

The UVAI is then calculated as in equation (A-1). In this approximation neither clouds nor surface effects are explicitly included in the radiative transfer calculations.

A.2 Modified LER Approximation

Atmos. Meas. Tech. Discuss., https://doi.org/10.5194/amt-2017-429
Manuscript under review for journal Atmos. Meas. Tech.
Discussion started: 20 December 2017

Atmospheric Measurement Techniques Discussions

In this approximation, surface and cloud reflected radiance (I_λ^s and I_λ^C , respectively) are explicitly accounted for but still assuming a molecular-only atmosphere. The I_λ^s terms are calculated using wavelength independent values of surface albedo of 0.08. The I_λ^C terms, on the other hand, are modeled by representing the cloud as a reflecting, opaque surface at located pressure P_t (cloud top) determined from existing climatologies and reflectivity (R_c) 0.80. In this approach, a wavelength independent cloud fraction is calculated as

$$f = \frac{I_{\lambda_0}^{obs} - I_{\lambda_0}^s}{I_{\lambda_0}^C - I_{\lambda_0}^s} \quad \text{(A-4)}$$

For f values less than or equal 1.0, I_λ^{cal} values are obtained from the expression

$$I_\lambda^{cal} = (1.0 - f)I_\lambda^s + fI_\lambda^C \quad \text{(A-5)}$$

and UVAI is then calculated from equation (A-1).

If $f > 1.0$, overcast sky conditions are assumed, and the SLER method of calculating I_λ^{cal} is used.